PHILOSOPHICAL TRANSACTIONS OF THE ROYAL SOCIETY A

Phil. Trans. R. Soc. A (2011) **369**, 3497–3509
doi:10.1098/rsta.2011.0100

Nonlinear plasmonics at planar metal surfaces

By Stefano Palomba[1], Hayk Harutyunyan[1], Jan Renger[2], Romain Quidant[2], Niek F. van Hulst[2] and Lukas Novotny[1,*]

[1]*Institute of Optics, University of Rochester, Rochester, New York, NY 14620-4040, USA*
[2]*ICFO-Institut de Ciencies Fotoniques, Mediterranean Technology Park, 08860 Castelldefels (Barcelona), Spain*

We investigate the nonlinear optical response of a noble metal surface. We derive the components of the third-order nonlinear susceptibility and determine an absolute value of $\chi^{(3)} \approx 0.2\,\mathrm{nm}^2\,\mathrm{V}^{-2}$, a value that is more than two orders of magnitude larger than the values found for typical nonlinear laser crystals. Using nonlinear four-wave mixing (4WM) with incident laser pulses of frequencies ω_1 and ω_2, we generate fields oscillating at the nonlinear frequency $\omega_{4\mathrm{WM}} = 2\omega_1 - \omega_2$. We identify and discuss three distinct regimes: (i) a regime where the 4WM field is propagating, (ii) a regime where it is evanescent, and (iii) a regime where the nonlinear response couples to surface plasmon polaritons.

Keywords: nonlinear optics; metamaterials; nonlinear plasmonics; nanophotonics; nonlinear frequency mixing; four-wave mixing

1. Introduction

During the past decade, the *linear* dielectric properties of noble metals have been exploited for a broad range of plasmonic applications, ranging from integrated circuits and energy harvesting to biosensing [1,2]. On the other hand, the *nonlinear* properties of metal nanostructures have received much less attention and are only now being studied. Because of their high intrinsic nonlinearities, metal nanostructures open up the possibility of performing a signal conversion in reduced dimensions, with potential applications ranging from on-chip frequency conversion/amplification to optical processing in nanoscale structures. Among the nonlinear processes studied so far are second-harmonic generation [3,4], third-harmonic generation [5], two-photon excited luminescence (TPL) [6–9], index modulation [10] and four-wave mixing (4WM) [11,12].

Efficient optical frequency conversion typically requires the nonlinear response from individual atoms or molecules to be summed up coherently, a process referred to as phase matching. This task is usually accomplished in nonlinear crystals of many wavelengths in size. However, future applications in nanophotonics require frequency conversion in materials with reduced dimensions, such as interfaces or discrete particles, for which phase matching is no longer possible. Nanoscale frequency conversion, therefore, relies on the intrinsic nonlinearities of materials.

*Author for correspondence (novotny@optics.rochester.edu).

One contribution of 9 to a Theo Murphy Meeting Issue ‘Metallic metamaterials and plasmonics’.

Using nonlinear 4WM, we have recently measured the third-order nonlinear susceptibility for noble metals and derived a value of $\chi^{(3)} = 0.2\,\mathrm{nm}^2\,\mathrm{V}^{-2}$ for gold [13]. Interestingly, this value is more than two orders of magnitude larger than the value of nonlinear crystals such as $LiNbO_3$ [14]. For a strong nonlinear response, it is necessary to couple incident radiation efficiently into the nonlinear material, but, as metals are reflective, only a small portion of the incident fields contribute. Therefore, for a strong nonlinear response, it is necessary to structure the surfaces such that the in-coupling and out-coupling of radiation is optimized [13]. To understand the nonlinear light–matter interaction with metals, we here consider the simplest possible configuration, namely a planar metal surface. For this geometry, the in-coupling and out-coupling of radiation can be represented in terms of Fresnel coefficients and the elements of the nonlinear susceptibility tensor become accessible through polarization measurements. We will demonstrate that the nonlinear response can be divided into three distinct regimes, namely a regime that leads to re-radiation of the nonlinear response, a regime where the nonlinear response is purely evanescent and a regime where the nonlinear response couples to surface modes.

2. Theory of nonlinear four-wave mixing

Optical 4WM uses two incident laser beams with frequencies ω_1 and ω_2 to produce radiation at frequency

$$\omega_{4\mathrm{WM}} = 2\omega_1 - \omega_2. \tag{2.1}$$

Our experiments are schematically depicted in figure 1*a*, which shows two incident beams at angles θ_1 and θ_2 with respect to the surface normal, and an outgoing beam at angle $\theta_{4\mathrm{WM}}$. Because of the translational invariance, the in-plane momentum is conserved, which yields

$$\frac{\omega_{4\mathrm{WM}}}{c}\,\sin\theta_{4\mathrm{WM}} = \frac{\omega_2}{c}\sin\theta_2 - 2\,\frac{\omega_1}{c}\sin\theta_1. \tag{2.2}$$

Combining equations (2.1) and (2.2) yields a relationship between the outgoing angle $\theta_{4\mathrm{WM}}$ and the incoming angles θ_1 and θ_2. It turns out that $\theta_{4\mathrm{WM}}$ can be either real or imaginary. In the former case, the 4WM field is propagating (outgoing wave) whereas in the latter case it is evanescent.

The incident beams can be represented in complex form as

$$\mathbf{E}_i = \mathrm{E}_i^o \begin{bmatrix} -\cos\theta_i \sin\phi_i t_p(\theta_i) \\ \cos\phi_i\, t_s(\theta_i) \\ \sin\theta_i \sin\phi_i t_p(\theta_i) \end{bmatrix} \mathrm{e}^{\mathrm{i}[\mathbf{k}_i\cdot\mathbf{r}-\omega_i t]}, \tag{2.3}$$

where t_s and t_p are the Fresnel transmission coefficients for s and p polarized incident light, respectively, and E_i^o is the amplitude of the incident field. ϕ_i is the polarization angle and $\mathbf{k}_i = (-k_i \sin\theta_i, 0, k_i\cos\theta_i)$ is the wavevector. The incident fields give rise to a nonlinear polarization $\mathbf{P} = (P_x, P_y, P_z)$ according to

$$\mathbf{P} = \varepsilon_o \chi^{(3)}(-\omega_{4\mathrm{WM}}; \omega_1, \omega_1, -\omega_2)\mathbf{E}_1\mathbf{E}_1\mathbf{E}_2^*, \tag{2.4}$$

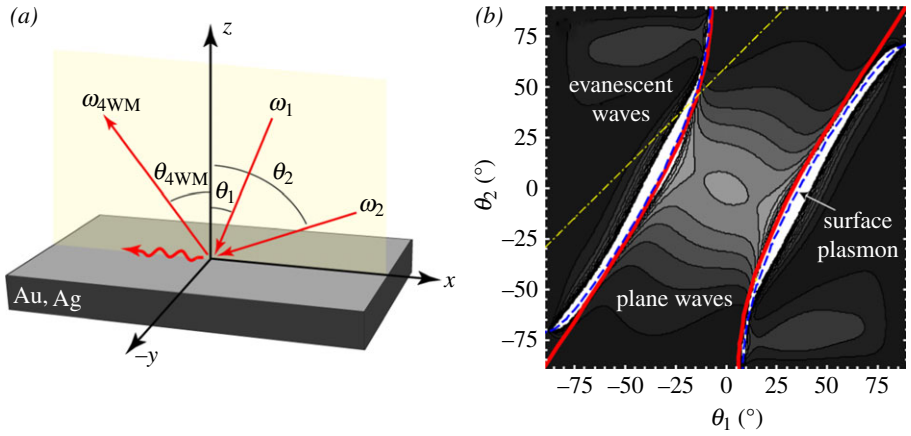

Figure 1. Nonlinear 4WM at a planar gold surface. (*a*) Illustration of the experiments. Two incident laser beams with frequencies ω_1 and ω_2 give rise to a 4WM field oscillating at the frequency $\omega_{4WM} = 2\omega_1 - \omega_2$. (*b*) Intensity of 4WM at the metal surface for $\lambda_1 = 707$ nm and $\lambda_2 = 800$ nm. Depending on the incident angles θ_1 and θ_2 different modes can be excited: (i) propagating waves at angle θ_{4WM}, (ii) evanescent waves confined to the metal surface, and (iii) surface plasmon polaritons. (Online version in colour.)

where $\chi^{(3)}$ is the third-order nonlinear susceptibility, a tensor of rank four. The nonlinear polarization defines a secondary source current that generates a field $\mathbf{E}_{4WM}$ oscillating at frequency ω_{4WM}. A straightforward theoretical analysis yields the following expressions for the field $\mathbf{E}_{4WM}$

$$\mathbf{E}_{4WM} = \frac{1}{2\,\varepsilon_o}\,\frac{1}{\sqrt{\varepsilon_1\,\varepsilon_2}}\left[\frac{k_{4WM,z} - k_{\downarrow,z}}{k_\downarrow^2 - k_{4WM}^2}\right] e^{i[\mathbf{k}_\uparrow\cdot\mathbf{r} - \omega_{4WM}t]} \times \begin{bmatrix} t_p(\theta_{4WM})(k_{\downarrow,z}P_x - k_{\downarrow,x}P_z) \\ \sqrt{\dfrac{\varepsilon_1}{\varepsilon_2}}\left(\dfrac{k_\downarrow^2}{k_{\uparrow,z}}\right) t_s(\theta_{4WM})P_y \\ -\left(\dfrac{k_{\uparrow,x}}{k_{\uparrow,z}}\right) t_p(\theta_{4WM})(k_{\downarrow,z}P_x - k_{\downarrow,x}P_z) \end{bmatrix}. \tag{2.5}$$

Here, $k_\uparrow^2 = \varepsilon_1\,(\omega_{4WM}/c)^2$ and $k_\downarrow^2 = \varepsilon_2(\omega_{4WM}/c)^2$, with ε_1 being the dielectric constant of the upper medium and $\varepsilon_2(\omega_{4WM})$ being the dielectric constant of gold. Because of momentum conservation along the interface, we have $k_{4WM,x} = k_{\downarrow,x} = k_{\uparrow,x}$. Equation (2.2) implies that $k_{4WM,x} = 2k_{1,x} - k_{2,x}$, and since $k_{1,y} = k_{2,y} = 0$ we also have $k_{4WM,y} = k_{\downarrow,y} = k_{\uparrow,y} = 0$. $t_s(\theta_{4WM})$ and $t_p(\theta_{4WM})$ are the Fresnel transmission coefficients for the outgoing fields at the 4WM frequency.

Figure 1*b* shows the calculated 4WM intensity $|\mathbf{E}_{4WM}|^2$ at a gold surface as a function of the incident angles θ_1 and θ_2. The incident wavelengths are chosen to be $\lambda_1 = 707$ nm and $\lambda_2 = 800$ nm, respectively. The figure shows that, depending on the incident angles, different modes can be excited at the 4WM frequency $\lambda_{4WM} = 633$ nm. Plane waves propagating at an angle θ_{4WM} are excited in the angular region bordered by the solid curves. Outside this region, the 4WM angle θ_{4WM}

becomes imaginary and the 4WM field is evanescent. Finally, surface plasmons are excited when the in-plane wavevector of the 4WM field corresponds to the wavevector of these surface polaritons

$$k_{spp} = \frac{\omega_{4WM}}{c}\sqrt{\frac{\varepsilon_1\ \varepsilon_2(\omega_{4WM})}{\varepsilon_2(\omega_{4WM}) + \varepsilon_1}}. \tag{2.6}$$

The dashed curves in figure 1*b* indicate the loci for which the evanescent waves couple to surface plasmon polaritons (SPPs). For points along this curve, the left-hand side of equation (2.2) can be replaced by equation (2.6).

3. Experimental results

In the following, we separately discuss the different 4WM regimes and present recent experimental data in support of our theoretical analysis.

(*a*) *Propagating the four-wave mixing regime*

In our experiments, we use a Ti : sapphire (TiSa) laser providing pulses of duration approximately 200 fs and centre wavelength $\lambda_2 = 800$ nm and an optical parametric oscillator (OPO) providing pulses of similar duration and wavelength $\lambda_1 = 707$ nm. The beams are first expanded to 10 mm diameter and then focused by two lenses of focal length $f = 50$ mm on a gold surface with roughness 2.3 nm_{rms}, as determined by atomic force microscopy. The angle between the two laser beams is held fixed at $\theta_2 - \theta_1 = 60°$ and the laser pulses are made to overlap in time by use of a delay line. The spot diameters at the surface are approximately 4.5 µm and are spatially overlapping. We use two different detection angles, which are both fixed with respect to the angles of the excitation beams, namely $\theta_{det} = \theta_1 + 60°$ and $\theta_{det} = \theta_1 + 24°$. The scattered radiation is collected by $f = 50$ mm lenses, filtered by optical stop-band filters to reject light at the excitation frequencies, and then sent into a fibre-coupled spectrometer. Alternatively, the collected light is filtered by narrow-band bandpass filters and detected with a single-photon counting avalanche photodiode for intensity measurements.

Figure 2*a* shows spectra of the detected radiation for two different sets of excitation and detection angles. For both spectra, the excitation beams were tuned to $\lambda_1 = 2\pi c/\omega_1 = 707$ nm and $\lambda_2 = 2\pi c/\omega_2 = 800$ nm (see arrows in figure). The spectra are characterized by the 4WM peaks located to the blue and the red of the excitation beams. For simplicity, we will restrict our discussion to the 4WM line at $\lambda_{4WM} = 633$ nm. An optical stop-band filter blocking the wavelength range $\lambda = [670\,..\,830]$ nm has been used to suppress the excitation beams in the detection path. The peak at $\lambda = 800$ nm is due to incomplete suppression of one of the excitation beams. The 4WM peaks disappear when the pulses of the excitation beams are temporally detuned. It is important to notice that the spectra shown in figure 2*a* are essentially background free. While optical 4WM can also be measured on metal nanostructures such as particles [11] and roughened surfaces, these spectra usually feature a strong background owing to one-photon and two-photon excited photoluminescence [7]. Besides being essentially background-free, the radiation of the planar gold surface is highly directional and the angular emission can be tuned by sample rotation.

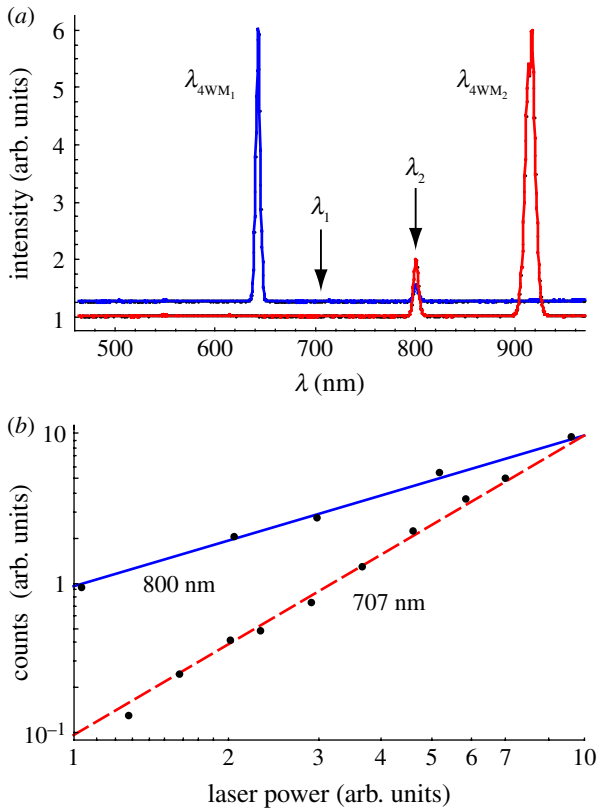

Figure 2. (*a*) Spectra of the detected radiation for two different sets of excitation detection angles. For both spectra, the excitation beams were tuned to $\lambda_1 = 707$ nm and $\lambda_2 = 800$ nm, respectively. The spectra show the two 4WM peaks at $\lambda_{4WM} = 633$ nm and $\lambda_{4WM} = 921$ nm and are nearly background free. The peak at 800 nm is due to incomplete suppression of the λ_2 excitation beam. Angles for $\lambda_{4WM} = 633$ nm: $\theta_1 = 6.9°$, $\theta_2 = 66.9°$, $\theta_{4WM_1} = 30.9°$. Angles for $\lambda_{4WM} = 921$ nm: $\theta_1 = -72.4°$, $\theta_2 = -12.4°$, $\theta_{4WM_2} = -6.4°$. (*b*) Dependence of the 4WM intensity at $\lambda_{4WM} = 633$ nm on excitation power. The lines indicate linear (slope = 1) and quadratic (slope = 2) behaviour. (Online version in colour.)

Figure 2*b* shows the experimental verification of the intensity dependence predicted by equation (2.4). The figure shows the 4WM intensity at $\lambda_{4WM} = 633$ nm as a function of excitation laser power. In accordance with theory, the 4WM intensity depends quadratically on the power of the $\lambda_1 = 707$ nm excitation and linearly on the power of the $\lambda_2 = 800$ nm excitation.

The outgoing angle θ_{4WM} is defined by the incoming angles θ_1 and θ_2 through equations (2.1) and (2.2). In our experiments, we hold the angle between the excitation beams fixed at $\theta_2 - \theta_1 = 60°$. To detect 4WM in the direction of $\theta_{det} = \theta_1 + 60°$ the incident angle needs to be adjusted to $\theta_1 = -5.4°$. Similarly, for a detection angle of $\theta_{det} = \theta_1 + 24°$, we calculate an excitation angle of $\theta_1 = +6.9°$. Our experimental results, shown in figure 3, yield peaks at $\theta_1 = -4.8°$ and $\theta_1 = +7.2°$ for the two detection angles, which are in good agreement with the theoretical predictions. To reject the ambient background and the incomplete suppression of the excitation beams (cf. figure 2*a*), we normalized the

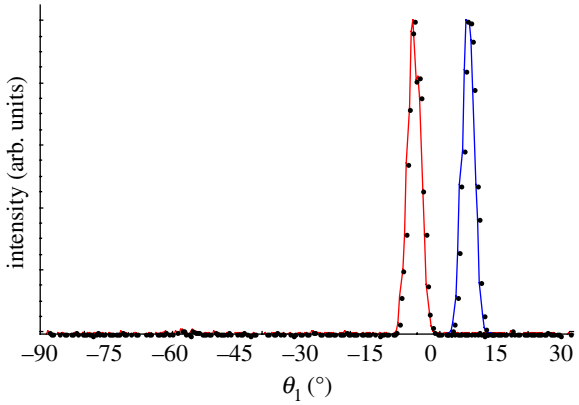

Figure 3. Measured 4WM intensity as a function of excitation angle θ_1. The detection directions are $\theta_{\mathrm{det}} = \theta_1 + 60°$ (left peak) and $\theta_{\mathrm{det}} = \theta_1 + 24°$ (right peak). The curves are scaled to the same peak value. (Online version in colour.)

measurements with the angular spectra recorded for temporally non-overlapping excitation pulses. The slight deviation of the experimental values from the theoretically predicted ones originates from calibration uncertainties and the angular dependence of the detection efficiency. The width of the peaks $\Delta\theta_1 \approx 4°$ originates from the fact that our excitation beams are not plane waves but focused beams with an angular range defined by the focusing lenses.

For isotropic materials such as gold, the 81 components of the third-order nonlinear susceptibility $\chi^{(3)}$ can be reduced to only three non-zero and independent components, namely $\chi^{(3)}_{1212}$, $\chi^{(3)}_{1221}$ and $\chi^{(3)}_{1122}$ [15]. Here, the indices '1' and '2' stand for any Cartesian index (x, y or z), with the condition that '1'≠'2'. The only other non-zero components are $\chi^{(3)}_{1111} = [\chi^{(3)}_{1212} + \chi^{(3)}_{1221} + \chi^{(3)}_{1122}]$. For the case of 4WM considered here, two of the incident fields are identical (see equation (2.4)) and hence $\chi^{(3)}_{1212} = \chi^{(3)}_{1122}$. To determine the relative magnitude and phase of the two susceptibilities $\chi^{(3)}_{1212}$ and $\chi^{(3)}_{1221}$, we measured the polarization dependence of the 4WM process. The results are shown in figure 4 for $\lambda_{4\mathrm{WM}} = 633\,\mathrm{nm}$ and for $\lambda_{4\mathrm{WM}} = 921\,\mathrm{nm}$. The latter results from the process $2\omega_2 - \omega_1$ (cf. figure 2*a*). The data points are superimposed to theoretical curves calculated using the theory outlined above. While the polarization angle ϕ of one of the incident beams is varied, the polarization of the other excitation beam is held fixed at $\phi = \pi/2$ (p-polarization) and the polarization of the detection path is held either at $\phi = \pi/2$ (dashed curves) or at $\phi = 0$ (solid curves).

For figure 4*a*, we used excitation angles of $\theta_1 = 6.9°$, $\theta_2 = 66.9°$ and a detection angle of $\theta_{\mathrm{det}} = 30.9°$, whereas the data in figure 4*b* were recorded with $\theta_1 = -72.4°$, $\theta_2 = -12.4°$ and $\theta_{\mathrm{det}} = -48.4°$. In order to bring theory and experiment in figure 4 into agreement, we used $\chi^{(3)}_{1221}/\chi^{(3)}_{1212} = 9$ in figure 4*a* and $\chi^{(3)}_{1221}/\chi^{(3)}_{1212} = -4$ in figure 4*b*. In both cases, $\chi^{(3)}_{1221}$ turns out to be the dominant term. The $\chi^{(3)}_{1212}$ term is only needed to account for the little 'wiggle' in the valleys of the dashed curve in figure 4*b*. Besides this wiggle, the dashed polarization curves follow predominantly a $\sin^4\phi$ dependence, whereas the solid curves have a $\sin^2(2\phi)$ dependence. This

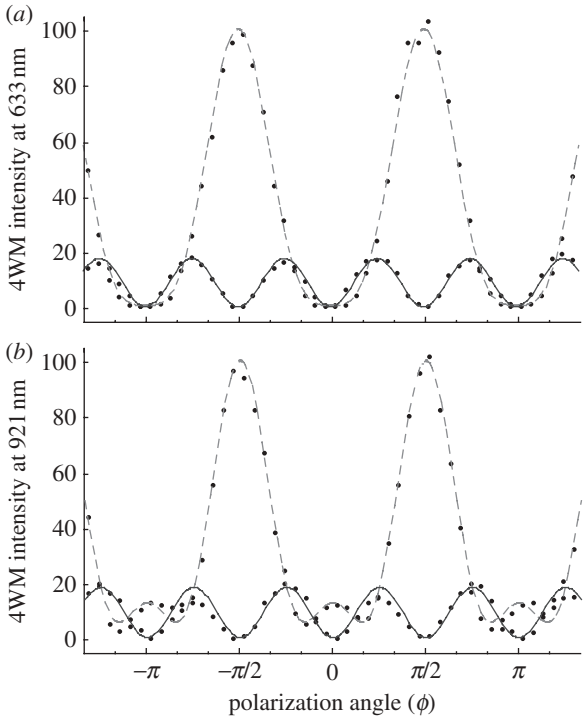

Figure 4. Polarization dependence of nonlinear 4WM. (*a*) Intensity of 4WM at $\lambda_{4WM} = 633$ nm as a function of the polarization angle of the $\lambda_1 = 707$ nm excitation beam. The polarization angle of the $\lambda_2 = 800$ nm beam is held fixed at $\phi = \pi/2$ (p-polarization). (*b*) Intensity of 4WM at $\lambda_{4WM} = 921$ nm as a function of the polarization angle of the $\lambda_2 = 800$ nm excitation beam. The polarization angle of the $\lambda_1 = 707$ nm beam is held fixed at $\phi = \pi/2$ (p-polarization). The detection polarization is switched between $\phi = 0$ (s-polarization, solid curves) and $\phi = \pi/2$ (p-polarization, dashed curves). Black dots are data and solid lines are theoretical curves.

behaviour follows directly from the power dependence of the 4WM processes (cf. figure 4*b*). The deviation between the values derived for the two different 4WM processes is ascribed to dispersion; interband transitions affect the $\lambda_{4WM} = 633$ nm stronger than $\lambda_{4WM} = 921$ nm. Interestingly, the polarization dependence of 4WM at $\lambda_{4WM} = 921$ nm yields a phase difference of π between $\chi^{(3)}_{1221}$ and $\chi^{(3)}_{1212}$. To measure the evolution of this phase difference, one would need to perform polarization-resolved measurements over an extended frequency range.

(*b*) *Evanescent four-wave mixing regime*

According to figure 1*b*, a considerable range of excitation angles (θ_1, θ_2) gives rise to evanescent 4WM fields. To explore the evanescent regime, we use an objective (numerical aperture (NA) = 1.3) with a large back aperture (13 mm) to focus both incident laser beams and to detect the emitted 4WM radiation. The set-up is illustrated in figure 5*a*. Small beam diameters are employed to control the incident angle of the excitation fields. The incident angles are measured by projecting the beams on a thermoelectrically cooled charge coupled device (CCD). Thus, the displacement Δx of the detected spot on the CCD measured from the

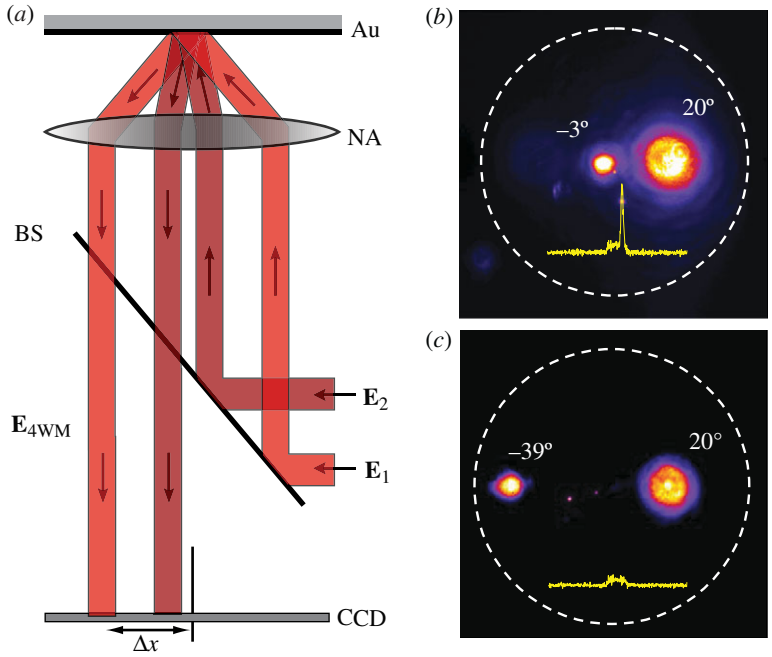

Figure 5. Pupil plane imaging. (*a*) Illustration of the measurement procedure. Two incident laser beams of wavelengths $\lambda_1 = 800\,\text{nm}$ and $\lambda_2 = 1150\,\text{nm}$ are reflected by a beamsplitter (BS) and sent into an objective (NA = 1.3) with a large back aperture. The beam position in the pupil plane defines the incident angle on the sample according to $\theta = \arcsin(\Delta x/f)$, with f being the focal length of the objective. (*b*,*c*) Pupil plane images. While one of the beams (ω_2) is held fixed at a position that corresponds to an incident angle of $\theta_2 \approx 20°$, the other beam is positioned at different locations spanning the angular range $\theta_1 \approx -39°..20°$. For all locations, the emitted radiation is detected and spectrally analysed (insets). For large θ_1, the 4WM wave is evanescent and no 4WM is detected. (Online version in colour.)

optical axis is a direct measure for the angle of incidence $\theta = \arcsin(\Delta x/f)$, with f being the focal length of the objective [16], and the incident beam size determines the angular resolution of the system and the spot size on the gold surface.

The in-plane momentum of the 4WM wave excited by the two incident beams is defined by the left-hand side of equation (2.2). The normal component of the 4WM momentum is then calculated according to

$$k_{\uparrow,z} = \sqrt{\varepsilon_1 \frac{\omega_{4\text{WM}}^2}{c^2} - \varepsilon_1 \left[\frac{\omega_2}{c}\sin\theta_2 - 2\,\frac{\omega_1}{c}\sin\theta_1\right]^2}, \tag{3.1}$$

where c is the speed of light and ε_1 is the (non-dispersive) dielectric constant of the medium from which the two exciting fields are incident. The loci for which $k_{4\text{WM,z}} = 0$ are shown as solid curves in figure 1*b*. They divide the evanescent 4WM region from the propagating one.

To demonstrate the transition from the propagating to the evanescent 4WM regime, we fix one of the incident beams in the back focal plane of the objective and step the other beam between different positions while recoding the spectrum

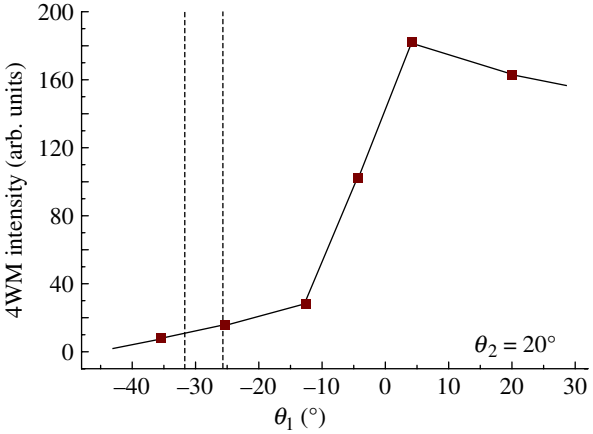

Figure 6. Plot of the emitted 4WM intensity recorded as a function of the incident angle θ_1. θ_2 is held fixed at $\approx 20°$. The incident beams have wavelengths $\lambda_1 = 800\,\text{nm}$ and $\lambda_2 = 1150\,\text{nm}$ and generate 4WM at $\lambda_{4\text{WM}} = 612\,\text{nm}$. For $\theta_1 = -26.5°$, the 4WM field propagates outside the angular range of the objective. For angles beyond $\theta_1 = -32.5°$ the 4WM field is evanescent. (Online version in colour.)

of the emitted 4WM radiation. Images of the back focal plane are rendered in figure 5*b*,*c*. The insets in the figure show the spectra of the emitted radiation. In figure 5*b*, the incident angles are in the propagating regime giving rise to emitted radiation with a 4WM peak (inset). In figure 5*c*, the incident angles are in the evanescent regime and no 4WM is registered. The small bump in the spectrum is a TPL background [7]. The measured 4WM intensity as a function of the angular displacement is plotted in figure 6.

The ability to generate evanescent 4WM fields radiatively is attractive for various optical applications. For example, the 4WM energy bound to the surface can be coupled to optoelectronic structures, such as waveguides and couplers, or it can be employed as a background-free source for dark-field imaging [17]. Notice that the excitation of evanescent 4WM fields is not restricted to metal surfaces and that the same excitation scheme works for any material with a nonlinear third-order susceptibility.

(*c*) *Coupling to surface plasmon polaritons*

The efficiency of 4WM is the highest when the in-plane wavevector of the 4WM wave coincides with the wavevector of the SPP defined in equation (2.6) (cf. figure 1*b*). The reason is that the excitation of SPPs gives rise to a longer interaction time between incident radiation and metal surface, which results in a stronger nonlinear response. The momentum condition for surface plasmon excitation becomes

$$\frac{\omega_{4\text{WM}}}{c}\sqrt{\frac{\varepsilon_1\varepsilon_2(\omega_{4\text{WM}})}{\varepsilon_2(\omega_{4\text{WM}})+\varepsilon_1}} = \frac{\omega_2}{c}\sin\theta_2 - 2\,\frac{\omega_1}{c}\sin\theta_1, \tag{3.2}$$

which defines a condition between the two incident angles θ_1 and θ_2.

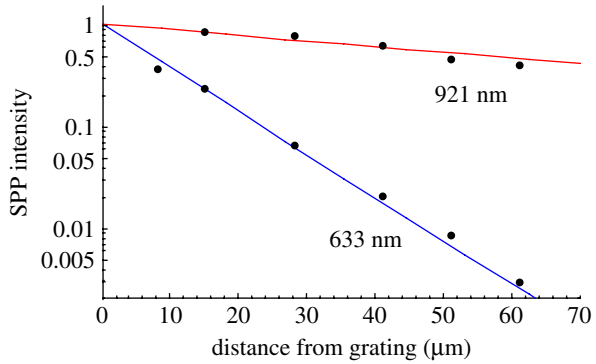

Figure 7. SPP decay for $\lambda_{4WM} = 633$ nm and $\lambda_{4WM} = 921$ nm. The data points (black dots) represent the measured SPP intensity as a function of the separation between the excitation spot and the grating used for out-coupling. The data are superimposed on the free SPP decay curves characterized by the decay lengths $L_{633} = 10.2\,\mu$m and $L_{921} = 78\,\mu$m, respectively. (Online version in colour.)

To prove the excitation of SPPs by nonlinear 4WM, we have fabricated gratings into the gold surface to convert the excited SPPs into propagating radiation. The latter is collected by $f = 50$ mm lenses, filtered by optical stop-band filters to reject light at the incident frequencies, and then sent into a fibre-coupled spectrometer. The gratings used for the out-coupling of SPPs consist of periodic grooves of depth 70 nm and width 150 nm, fabricated by electron beam lithography and reactive ion etching. We performed measurements for plasmons at both 4WM frequencies, $2\omega_1 - \omega_2$ and $2\omega_2 - \omega_1$. In our experiments, the centre wavelengths corresponding to ω_1 and ω_2 are chosen as $\lambda_1 = 707$ nm (OPO) and $\lambda_2 = 800$ nm (TiSa), respectively. The resulting 4WM frequencies correspond to the wavelengths $\lambda_{4WM} = 633$ nm and $\lambda_{4WM} = 921$ nm, respectively. Measurements were carried out for detection directions fixed with respect to the normal of the surface and for detection directions fixed with respect to the incident laser beams. Also, we varied the grating periods to verify that the findings are independent of the out-coupling conditions. In all configurations, we observed the same results.

Our experiments confirm the condition stated in equation (3.2) [18]. As before, the angle between the two excitation beams was fixed at $\theta_2 - \theta_1 = 60°$, which allows us to express plasmon excitation in terms of a single angle only. According to equation (3.2), to excite SPPs at a wavelength $\lambda_{4WM} = 633$ nm the incident angles need to be adjusted to $\theta_1 = -16.0°$ and $\theta_2 = +44.0°$. On the other hand, to excite SPPs at a wavelength $\lambda_{4WM} = 921$ nm we require $\theta_1 = -63.9°$ and $\theta_2 = -3.9°$. We place the excitation beams to the side of the fabricated gratings and record the outcoupled 4WM intensity as a function of incident angles. It has to be emphasized that the excitation beams do not interact with the gratings, i.e. the excitation spots are spatially separated from the gratings by several tens of micrometres. By varying the separation distance and measuring the outcoupled SPP intensity, we are able to record the SPP propagation length.

The theoretical values for the SPP propagation length at $\lambda_{4WM} = 633\,\text{nm}$ and $\lambda_{4WM} = 921\,\text{nm}$ are $L_{633} = 10.2\,\mu\text{m}$ and $L_{921} = 78\,\mu\text{m}$, respectively. On the other hand, for a gold film of 50 nm thickness, which is commonly used in the Kretschmann configuration, these values reduce by ≈ 35–50% owing to inevitable leakage radiation from the SPPs into the substrate. This reduction is eliminated by the 4WM excitation scheme because there is no need for evanescent wave coupling and no leaky waves are present. To measure the SPP propagation length, we record the SPP intensity as a function of the distance between the excitation spot and the grating used for out-coupling. The data are rendered in figure 7 together with the theoretical decay curves. The slight deviations originate from variations in the collection efficiency, i.e. when we displace the sample, we also move the out-coupling grating relative to the fixed collection lens. Also, the excited SPPs do not have planar wavefronts, which gives rise to further deviations from the theoretical curves. Nevertheless, the data are in good agreement with the expected behaviour and support our claim that the 4WM excitation scheme does not affect the free SPP propagation length.

4. Conclusions and outlook

We have studied 4WM at a planar gold surface and identified three distinct regimes, namely a regime where propagating radiation at the 4WM frequency is generated, a regime where the 4WM field is evanescent and a regime where the evanescent 4WM field couples to surface modes, such as SPPs. Typically, SPPs cannot be excited by propagating radiation and hence they are 'dark modes'. With our multi-photon excitation scheme, we overcome the limitations imposed by reciprocity and directly couple to dark modes. In principle, the multi-photon excitation scheme can be employed to excite any localized in-plane modes, such as waveguide modes, surface phonon polaritons or modes associated with two-dimensional electron gases, such as semiconductor heterojunctions.

Linear SPP excitation schemes, such as the Otto or Kretschmann configuration, are limited by reciprocity, in the sense that radiative excitation of SPPs also implies radiative decay of SPPs. This effect reduces the SPP propagation length as noted before. Furthermore, traditional SPP excitation requires specific sample preparation procedures, such as thin film deposition or fabrication of gratings or couplers, which often restricts the versatility and flexibility of devices. The nonlinear 4WM scheme described in this work overcomes these restrictions and allows SPPs to be launched on any metal surface by combining photons from two separate laser beams. On the other hand, the 4WM scheme has considerably lower efficiency. For typical excitation peak intensities of $\hat{I}_1 = 22\,\text{GW}\,\text{cm}^{-2}$ and $\hat{I}_2 = 46\,\text{GW}\,\text{cm}^{-2}$, we determine a SPP excitation rate of 10^9 plasmons per second. This value can be improved by several orders of magnitude by using higher intensities and excitation frequencies near the surface plasmon resonance (approx. 510 nm for a planar gold surface) [19]. It has to be emphasized that the plasmons excited by 4WM have a well-defined energy, momentum and directivity.

The efficiency of 4WM is defined by the third-order nonlinear susceptibility, which we determined to be $\chi^{(3)} = 0.2\,\text{nm}^2\,\text{V}^{-2}$, a value that is significantly higher than the values of typical nonlinear laser crystals. However, for efficient 4WM to occur the incident laser fields need to interact with the nonlinear material and

hence penetrate through the surface of the material. Because metals are reflective, most of the incident radiation does not make it into the bulk of the material. Therefore, to increase the efficiency, it is necessary to structure the surfaces such that the in- and out-coupling of radiation is facilitated. In this sense, the surface structures function as receiving and transmitting antennas. In principle, it is conceivable to structure the entire bulk material and to design a 'nonlinear metamaterial', which maximizes the interaction with incoming and outgoing radiation thereby providing an ultrastrong nonlinear response. The intrinsic material nonlinearity of such a material would remain unaltered, but owing to improved in- and out-coupling of radiation the overall nonlinear conversion efficiency would be strongly enhanced.

This work was funded by the National Science Foundation (ECCS-0918416), the Catalan AGAUR pivprogram and ICREA.

References

1 Atwater, H. A. & Polman, A. 2010 Plasmonics for improved photovoltaic devices. *Nat. Mat.* **9**, 205–213. (doi:10.1038/nmat2629)
2 Schuller, J. A., Barnard, E., Cai, W., Jun, Y. C., White, J. & Brongersma, M. L. 2010 Plasmonics for extreme light concentration and manipulation. *Nat. Mat.* **9**, 193–204. (doi:10.1038/nmat2630)
3 Bouhelier, A., Beversluis, M., Hartschuh, A. & Novotny, L. 2003 Near-field second-harmonic generation induced by local field enhancement. *Phys. Rev. Lett.* **90**, 13903. (doi:10.1103/PhysRevLett.90.013903)
4 Labardi, M., Allegrini, M., Zavelani-Rossi, M., Polli, D., Cerullo, G., Silvestri, S. D. & Svelto, O. 2004 Highly efficient second-harmonic nanosource for near-field optics and microscopy. *Opt. Lett.* **29**, 62–64. (doi:10.1364/OL.29.000062)
5 Lippitz, M., van Dijk, M. A. & Orrit, M. 2005 Third-harmonic generation from single gold nanoparticles. *Nano Lett.* **5**, 799–802. (doi:10.1021/nl0502571)
6 Bouhelier, A., Beversluis, M. R. & Novotny, L. 2003 Characterization of nanoplasmonic structures by locally excited photoluminescence. *Appl. Phys. Lett.* **83**, 5041–5043. (doi:10.1063/1.1634383)
7 Beversluis, M. R., Bouhelier, A. & Novotny, L. 2003 Continuum generation from single gold nanostructures through near-field mediated intraband transitions. *Phys. Rev. B* **68**, 115433. (doi:10.1103/PhysRevB.68.115433)
8 Schuck, P. J., Fromm, D. P., Sundaramurthy, A., Kino, G. S. & Moerner, W. E. 2005 Improving the mismatch between light and nanoscale objects with gold bowtie nanoantennas. *Phys. Rev. Lett.* **94**, 017402. (doi:10.1103/PhysRevLett.94.017402)
9 Ghenuche, P., Cherukulappurath, S., Taminiau, T. H., van Hulst, N. F. & Quidant, R. 2008 Spectroscopic mode mapping of resonant plasmon nanoantennas. *Phys. Rev. Lett.* **101**, 116805. (doi:10.1103/PhysRevLett.101.116805)
10 MacDonald, K. F., Samson, Z. L., Stockman, M. I. & Zheludev, N. I. 2008 Ultrafast active plasmonics. *Nat. Photonics* **3**, 55–58. (doi:10.1038/nphoton.2008.249)
11 Danckwerts, M. & Novotny, L. 2007 Optical frequency mixing at coupled gold nanoparticles. *Phys. Rev. Lett.* **98**, 026104. (doi:10.1103/PhysRevLett.98.026104)
12 Palomba, S. & Novotny, L. 2008 Nonlinear excitation of surface plasmon polaritons by four-wave mixing. *Phys. Rev. Lett.* **101**, 056802. (doi:10.1103/PhysRevLett.101.056802)
13 Renger, J., Quidant, R., Hulst, N. V. & Novotny, L. 2010 Surface enhanced nonlinear four-wave mixing. *Phys. Rev. Lett.* **104**, 046803. (doi:10.1103/PhysRevLett.104.046803)
14 Ganeev, R. A., Kulagin, I. A., Ryasnyansky, A. I., Tugushev, R. I. & Usmanov, T. 2003 Characterization of nonlinear optical parameters of KDP, $LiNbO_3$ and BBO crystals. *Opt. Commun.* **229**, 403–412. (doi:10.1016/j.optcom.2003.10.046)

15 Boyd, R. W. 2008 *Nonlinear optics*, 3rd edn. San Diego, CA: Academic Press.
16 Bouhelier, A., Ignatovich, F., Bruyant, A., Huang, C., des Francs, G. C., Weeber, J. C., Dereux, A., Wiederrecht, G. P. & Novotny, L. 2007 Surface plasmon interference excited by tightly focused laser beams. *Opt. Lett.* **32**, 2535–2537. (doi:10.1364/OL.32.002535)
17 Harutyunyan, H., Palomba, S., Renger, J., Quidant, R. & Novotny, L. 2011 Nonlinear dark-field microscopy. *Nano Lett.* **10**, 5076–5079.
18 Renger, J., Quidant, R., Hulst, N. V., Palomba, S. & Novotny, L. 2009 Free-space excitation of propagating surface plasmon polaritons by nonlinear four-wave mixing. *Phys. Rev. Lett.* **103**, 266802. (doi:10.1103/PhysRevLett.103.266802)
19 Liao, H. B., Xiao, R. F., Fu, J. S., Wang, H., Wong, K. S. & Wong, G. K. L. 1998 Origin of third-order optical nonlinearity in Au:SiO_2 composite films on femtosecond and picosecond time scales. *Opt. Lett.* **23**, 388–390. (doi:10.1364/OL.23.000388)